Wang Hao
Cheng Yuan-Sheng
Pei Da-Ming
Hao Wei-Wei
Gan Lin

http://dx.doi.org/10.21278/brod70203

ISSN 0007-215X
eISSN 1845-5859

WATER ENTRY HYDROELASTICITY ANALYSIS OF LATTICE SANDWICH PANEL WITH IMPERFECTION: SIMULATION AND ENGINEERING MODEL

UDC 62-419.5:629.5.015.4
Professional paper

Summary

In the present work, the three dimensional (3D) hydroelasticity characteristics of imperfect lattice sandwich panel (ILSP) subjected to water entry via analytical prediction and numerical simulations are proposed. Firstly, numerical investigations are performed on water entry characteristics based on Arbitrary Eulerian-Lagrange (ALE) coupling method for modeling fluid-structure interaction (FSI) at an impact velocity of 5.0m/s. The results show the impact pressure on total FSI surface of ILSP is generally lower than that of the perfect lattice sandwich panel. Then a novel semi-analytical method to calculate the elastic constants of ILSP is introduced. Based on this approach, an engineering computational model is developed to predict the deformation of ILSP, in which the total deformation is separated into two parts; local field deformation and global field deformation. Good agreement between the numerical and analytical results is achieved. And the effects of geometric parameters such as the thickness of face sheet, height of ILSP and relative density of core are discussed.

Key words: *Imperfect lattice sandwich panel; Hydroelasticity; Fluid-structure interaction; Water entry*

Nomenclature

ILSP	Imperfect lattice sandwich panel	K_1 ,K_2	Dynamic coefficients
RM-ILSP	Random Moved ILSP	p_{max}	Peak impulsive pressure
PM-ILSP	Partly Moved ILSP	C_0	Sound speed of air
$2\tau_s$	Duration of water entry loading	$w_{max,G}$	Maximum global deflection of ILSP
f_s	Natural vibration frequency	$w_{max,L}$	Maximum local deflection of ILSP
a, b	Length (width) of structures	ρ_s	Density of base solid material

M_s	Mass of structures	p_∞	Atmosphere pressure,
t_f, t_b	Top (bottom) face sheet thickness	A, B	Empirical parameters
H_c	Height of core	ρ_w	Initial density of fresh water
$t_c \times t_c$	Section cross area of core	E_w	Specific internal energy per unit mass
v	Water entry velocity	a_1,a_2,a_3	Constants for the fluid
φ	Angle between face sheet and truss	b_0, b_1	Constants for the fluid
d_{c1}	Core cell length	ρ_a	Density of air
d_{c2}	Core cell width	γ	Heat capacities of the gas
E^*	Equivalent young modulus of ILSP	G^*	Equivalent shear modulus of ILSP
ρ_0	Relative density of core	η	Missing percents
C^*_G	Transverse shear rigidity matrix	D_f	Bending stiffness of face sheets
D^*_1	Bending rigidity ILSP lattice core	v^*	Poisson ratio
k	Missing percentage parameters	E_a	Specific internal energy of air
P_{perfect}	Pressure for perfect sandwich panel	$P_{\text{imperfect}}$	Pressure for imperfect sandwich panel
T_{LP}	Loading period	T_{NP}	First wet natural period of vibration
$p_{\max,L}$	Central FSI surface peak pressure	$p_{\max,G}$	Global FSI surface peak pressure

1. Introduction

It has been revealed that slamming on ship bow section may cause serious damages. Thus, in the conceptual design of ship and offshore structures, the prediction of hydrodynamic pressure acting on an impacting body is very important. Early in 1929, Von Karman [1] firstly introduced a significant contribution on this subject. Following Karman's classic works on hull-water impact, a series of studies on the theoretical analysis of water entry problem have been reported (Wagner [2], Kapsenberg [3], Faltinsen [4-5] Morabito [6], Korobkin [7-8] and Abrate [9] *et al*.). Due to the complexities of this problem (such as multi-physics interaction phenomenon, free surface tracking *et al*), only a few special cases of wedges entry water vertically at a constant velocity can be solved analytically. So, water entry problem has been solved by some different numerical methods (e.g. Boundary Element Method (BEM) [10-11], Arbitrary Lagrange-Euler Method (ALE) [12-13], Volume of Fluid Method (VOF) [14-16], Smoothed Particle Hydrodynamics (SPH) [17-18], *et al*).

Most of previous investigations concern on the traditional ship and offshore structures such as flat plate [19], stiffened panel [20-21], V-type wedges [22-24], spherical ball [25-26], cylindrical projectile [26] and propeller blade wedge section [27] *et al*. In these studies, the common perspective of water entry phenomenon is a typical FSI problem. Obviously, the elasticity of the structures is expected to influence the results of this problem (here, which calls "hydroelasticity"). Some impressive investigations concern on the role of hydroelasticity when this effect is significant. Jones may be the first person to discuss this topic [28]. After that, Berezniski [29] performed an impressive review of hydroelastic behaviour for Wagner-type impact by using explicit FEM code LS-DYNA. Then, Stenius [30-31] also illustrated the hydroelastic effects are typically characterized by a relation between loading period and natural period of vibration of the structure. Based on model experiments and numerical hydroelastic analysis results of the symmetric wedges (made by composite materials), Panciroli *et al*. [32-34] showed that the hydroelastic effects are negligible when the ratio between the wetting impact time and the first wet natural period is greater than 5. However, most of these hydroelastic interaction investigations are limited in simple steel structures.

More recently, the interest of sandwich structures with various lattice core topologies has grown rapidly for their significant advantages of light weight, high specific stiffness and strength [35-37]. The static and dynamic mechanical behaviour of sandwich structures with lattice truss core is quite different from other traditional constructions, including those with honeycomb core or corrugated core. In the most previous studies, the static mechanism and energy absorption behaviour of sandwich structures with lattice truss core subjected to air explosion, underwater explosion and fragment penetration are widely concerned [38-42]. Up to date, water entry characteristics of sandwich structures with lattice truss core have rarely been studied. In our previous work [43], the dynamic responses of perfect lattice sandwich panel (PLSP) under water entry are investigated. But due to the manufacturing reasons, defects in the lattices may be either in the form of vacancies, owing to missing trusses, or topological imperfections owing to displaced nodes. Thus, we shall explore theoretically and numerically the hydroelastic mechanism of imperfect lattice sandwich panel (ILSP) based on some simple cases [44].

In the present study, the hydroelasticity characteristics of imperfect lattice sandwich panel (ILSP) are further discussed. A new computational method is utilized for determination of the vibration performance of ILSP (the random moved missing and partly moved missing cases are both considered here). And these two models are validated by comparing against vibration numerical analysis. Furthermore, in order to calculate the global deflection of partly moved missing ILSP, a novel computational method is derived by adopting the simple support boundary assumption for missing area [44]. Results from this proposed model agree well with those from the 3D FSI analysis. Then, the geometric parameters effects of ILSP such as the thickness of face sheet, the relative density of core, the height of ILSP core *et al*. are also examined. The proposed model may be considered as initial point for modeling the design of the lattice sandwich structures subjected to water entry.

2. Geometric Characteristics of Imperfection Lattice Sandwich Panel (ILSP)

2.1 Descriptions of Imperfection Lattice Sandwich (ILSP)

In the practical cases, the imperfection of manufacture widely exists. Generally, there are three types imperfection in manufacture process including the core truss missing, initial wave less buckling of core truss, jointing invalidation between trusses and face sheet. And the core truss missing may be the most important. Thus, this type imperfection is considered here. Based on our previous studies [43-44], when the non-dimensional criteria $2\tau_s f_s$>4 (here, $2\tau_s$ is the duration of water entry loading, f_s is the natural vibration frequency of structure including added mass effect) the hydroelastic effect of lattice sandwich panel is not significant. In the present paper, both $2\tau_s f_s$>4 and $2\tau_s f_s$<4 are considered. Some other researchers also give similar criteria to analysis the hydroelasticity of simple structures. Considering the added mass of the first vibration modal of structure for a v-shaped ship section, a similar definition given by Stenius *et al*. [30-31] is the ratio T_{LP} /T_{NP}. Where T_{LP} is the loading period based on the Wagner theory and T_{NP} is the first wet natural period of vibration. It is concluded that the hydroelastic effects are negligible and the response can be set as quasi-static for (T_{LP} /T_{NP})> 4. Here, by referring a practical monolithic flat panel of cruiser [43], the ILSP with an exposed area 595.1 mm × 270.5 mm is considered with $2\tau_s f_s$~5. Besides, the ILSP with an exposed area 1200.0 mm×1000.0 cm referred a stiffened plate of bulk carrier bottom structures is proposed with $2\tau_s f_s$~1.

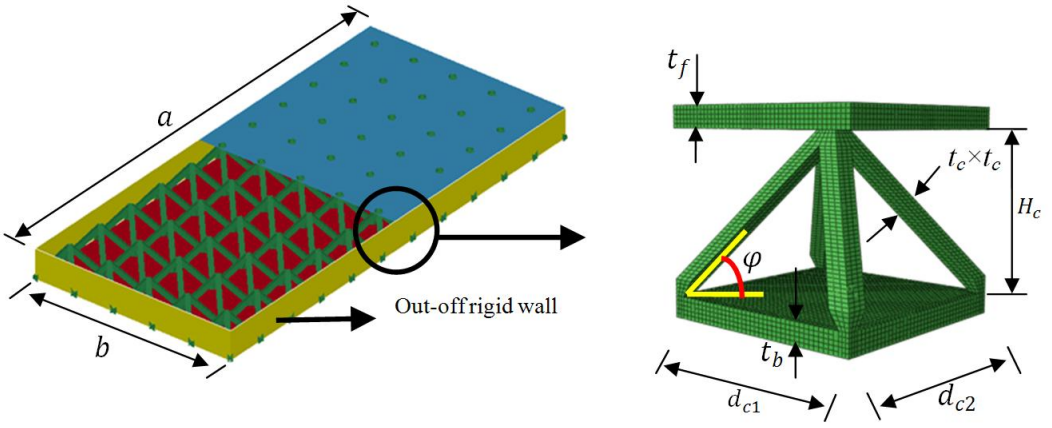

(a) Geometric parameter of lattice sandwich plate

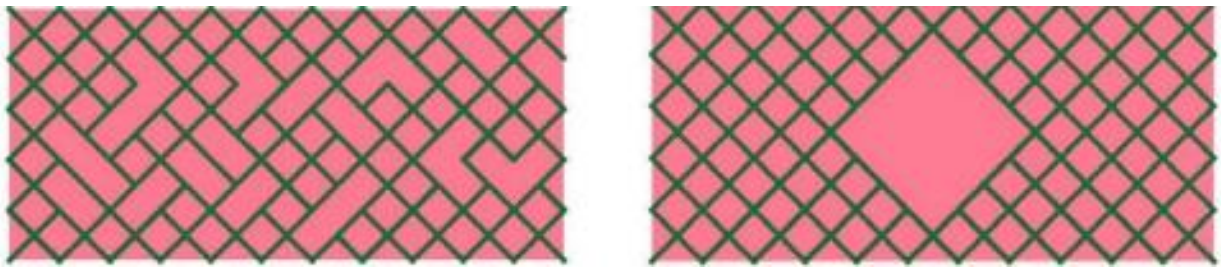

(b) Imperfection types

Fig. 1 Imperfect lattice sandwich Plate

2.1.1 $2\tau_s f_s$~5 (the hydroelastic effect is not significant)

Table 1 Computational cases when the hydroelastic effect is not significant

	a(cm)	b(cm)	φ	t_f(mm)	t_b(mm)	H_c(mm)	$t_c \times t_c$(mm×mm)	v(m/s)	Percents
C1	59.51	27.05	1.00	4.219	4.219	38.25	6.00×6.00	5m/s	0.00%
η(C2)=0.45%,η(C3)= 0.90%,η(C4)= 1.35%,η(C5)= 1.80%,η(C6)=3.60%, η(C7)= 5.40%,η(C8)= 9.09%,η(C9)= 9.54%,η(C10)= 10.91%,η(C11)= 16.36%.									

ILSP consists of two thin face sheets attached to both sides of a light weight lattice core with the total mass of perfect lattice core sandwich plate M_s=67.6kg, see [43-44]), and the geometric description of ILSP is plotted in detail in Fig. 1. Here, the geometric parameters of referenced case C1 are $\varphi=\pi/4$, $d_{c1}=d_{c2}=d_c$=54.100mm, t_f=4.219mm, t_b=4.219mm, t_c=6.000mm, H_c=38.250mm (for case C1, the lattice sandwich panel is perfect, please see Table 1). Two missing imperfection types are considered in this study; the first type is randomly moved missing imperfection, and the second type is partly moved imperfection. And the missing core cell (here it means the reduction in density) percentage varies from 0.45% to 16.36% (the cases C2~C11, please also see Table 1). The boundary condition of panel can be taken as clamped. Therefore, a sealed off round structure made by rigid materials (rigid out wall, see Fig. 1) is used to model clamped boundary condition. Particularly, for each random moved missing cases C2(R) ~ C11(R), the five random types are considered here. So, there are totally 50 random moved missing cases. For partly moved missing cases C2(P) ~ C11(P), to simplify the analysis, only the central partly moved missing is considered (see Fig. 1).

2.1.2 $2\tau_s f_s$~1.0 (the hydroelastic effect is significant)

In this case, the parameters of C1' are φ=49.88°, $d_{c1}=d_{c2}=d_c$=100.00mm, t_f=1.000mm, t_b=1.000mm, t_c=6.500mm, H_c=90.000mm (for case C1', the lattice sandwich panel is perfect,

please see Table 2). Two missing imperfection types are also considered in this study; the first type is randomly moved missing imperfection, and the second type is partly moved imperfection. The missing core cell (here it means the reduction in density) percentage varies from 0.45% to 16.36% (the cases C2'~C11', please see Table 2). The other conditions are same as $2\tau_s f_s$~5.

Table 2 Computational cases when the hydroelastic effect is significant

	a(cm)	b(cm)	φ(°)	t_f(mm)	t_b(mm)	H_c(mm)	$t_c \times t_c$(mm×mm)	v(m/s)	Percents
C1'	120	100	49.88	1.00	1.00	90.00	6.5×6.5	5m/s	0
η(C2')=0.42%,η(C3')= 0.83%,η(C4')= 2.50%,η(C5')= 4.16%,η(C6')=5.833%, η(C7')= 6.67%,η(C8')= 7.50%,η(C9')= 8.33%,η(C10')= 12.50%,η(C11')= 16.70%.									

3. Mathematical Formulation and Vibration Analysis of ILSP

3.1 Basics Solution Idea of ILSP Structural Dynamics Problem

3.1.1 Basics Solution Idea of Random Moved ILSP (RM-ILSP)

As the complexity of PM-ILSP, only the elastic constants of RM-ILSP are considered here. Due to the discrete stochastic characteristics, the homogenization method is adopted. According to the concept of continue damage mechanics (CDM), the elastic constants of RM-ILSP (E^*, G^*) are given as follows.

$$E^*, G^* \sim f(\varphi)\rho_0(1-\eta)^k \tag{1}$$

where $f(\varphi)$ is a dimensionless function of φ (the meaning of notation φ sees Fig. 1), ρ_0 is the relative density of RM-ILSP and k is a dimensionless constant (if η=0.00% means the perfect case).

$$E^*, G^* \sim f(\varphi)\rho_0(1-\eta)^k \approx f(\varphi)\rho_0(1-k\eta) \tag{2}$$

Here, the dimensionless function $f(\varphi)$ and the relative density ρ_0 can be referred in literature,

$$f(\varphi) = \begin{cases} \sin^4\varphi & for\ E^* \\ \dfrac{1}{8}\sin^2(2\varphi) & for\ G^* \end{cases} \tag{3}$$

$$\rho_0 = \rho_s \frac{4lt_c^2}{d_c^2 \sin\varphi}(1-\eta) \tag{4}$$

where the meanings of t_c and d_c can be seen in Fig. 1, l is the length of core truss, and ρ_s is of base solid material for ILSP.

By combining Eqs. (1)-(4) and neglecting the high order terms in the Taylor expansions, the expression of E^* and G^* can be written as follows,

$$E^* = \rho_s \sin^3\varphi \frac{4lt_c^2}{d_c^2}\left[1-(k+1)\eta\right],\ \ G^* = \rho_s \frac{1}{2}\frac{\sin^2(2\varphi)lt_c^2}{d_c^2 \sin\varphi}\left[1-(k+1)\eta\right] \tag{5}$$

In the previous study, Wallach and Gibson [45] has given an observation that Young' modulus of lattice materials decreases linearly with increasing fraction of missing trusses, with a roughly 16.6% decrease in modulus for every 10% reduction in relative density. Thus, we assume that the value of k is set to be 0.66 here. If the equivalent elastic constants E^* and G^* are calculated, the response of RM-ILSP is easy to obtained based on our previous study [43-44] which is a classic structural dynamic problem in linear region.

3.1.2 Basics Solution Idea of Partly Moved ILSP (PM-ILSP)

In this section, the boundary condition of partly moved ILSP (PM-ILSP) is analyzed. If the missing percentage of core truss is relative large, the above method will not be suitable. Thus, the local boundary effect must be considered. Based on the previous study [43-44], it shows that the core truss can be set as supported by rows of equidistant trusses or simply supported edges. To simplify the analysis, the shape of partly moved area is set to be rectangular, making the calculation of the vibration and static behavior of local partly moved area much easier.

3.2 Vibration Verification Analysis of ILSP

If the equivalent elastic properties of random moved ILSP are obtained from Eqs. (1)-(5), the fundamental bending vibration frequencies of RM-ILSP are calculated by three steps [43] as follows. The first and second step is to calculate the equivalent shear (bending) rigidity of ILSP lattice core. And the last step is to calculate the natural frequency of RM-ILSP. In this key step, an approximate method [43-44, 46-47] is adopted to analyze the fundamental vibration frequency. And the detailed expressions of the formulations are shown as follows.

Step 1: calculate the equivalent shear rigidity of RM-ILSP lattice core [43]

$$C_G^* = \frac{\left[H_c + \left(t_f + t_b\right)/2\right]}{H_c}\begin{bmatrix} C_{55}^{*H} & C_{54}^{*H} \\ C_{45}^{*H} & C_{44}^{*H} \end{bmatrix} \tag{6}$$

where C^*_{G} is the transverse shear rigidity matrix of ILSP core (the detailed expressions of the homogenized module of lattice core $C_{\alpha\beta}{}^{*\mathrm{H}}$ (α, β=4, 5) can be found in literature [43]).

Step 2: calculate the bending rigidity ILSP lattice core [43]

$$D_1^* = \frac{E^*\left[\left(H_c + \left(t_f + t_b\right)\right)^3 - H_c^3\right]}{12\left(1-\nu^{*2}\right)} \times \left[1 - \frac{3\left(t_f - t_b\right)^2}{\left(1 + \frac{H_c}{H_c + \left(t_f + t_b\right)} + \frac{H_c + \left(t_f + t_b\right)}{H_c}\right)\left(t_f + t_b\right)^2}\right] \tag{7}$$

Here, for the thin face sheets of ILSP, only bending deformation is considered (the bending stiffness D_f of face sheets is included).

Step 3: calculate the natural frequency of ILSP [43].

The third step is to calculate the natural frequency of ILSP. In the present investigation, an approximate method is adopted to analyze the fundamental vibration frequency of the

ILSP. And the detailed steps of solving approximate equations can be found in our previous study [43] and classic literature [47].

Table 3 Vibration analysis of imperfect lattice sandwich plate

(a) Random missing case

η	1st (Analytical/FEM)		Error	2st(Analytical/FEM)		Error	3st (Analytical/FEM)		Error
0.00%	1691.1	1553.9	8.83%	1966.9	1858.9	5.81%	2421.2	2289.2	5.77%
0.45%	1660.3	1552.2	6.96%	1943.7	1862.2	4.38%	2411.3	2275.1	5.99%
0.90%	1654.1	1547.3	6.90%	1936.9	1851.6	4.61%	2408.2	2268.3	6.17%
1.35%	1647.8	1541.9	6.87%	1930.1	1841.0	4.84%	2399.9	2262.0	6.10%
1.80%	1641.6	1528.1	7.43%	1923.2	1838.0	4.64%	2391.5	2256.4	5.99%
3.60%	1616.3	1523.2	6.11%	1895.6	1827.6	3.72%	2367.8	2235.9	5.90%
5.40%	1590.7	1518.3	4.77%	1867.5	1799.3	3.79%	2333.5	2226.2	4.82%
9.09%	1538.2	1487.2	3.43%	1809.6	1746.6	3.61%	2262.6	2171.4	4.20%
9.54%	1531.5	1487.0	2.99%	1802.2	1746.0	3.22%	2253.6	2169.8	3.86%
10.91%	1511.3	1483.5	1.87%	1779.8	1741.5	2.20%	2226.1	2155.8	3.26%
16.36%	1427.4	1423.0	0.31%	1686.4	1681.9	0.27%	2111.4	2113.4	-0.09%

(b) Partly moved missing case

η	1st (Analytical/FEM)		Error	2st(Analytical/FEM)		Error	3st (Analytical/FEM)		Error
0.00%	1691.1	1553.9	8.83%	1966.9	1858.9	5.81%	2421.2	2289.2	5.77%
0.45%	1660.3	1553.4	6.88%	1943.7	1851.2	5.00%	2411.3	2288.5	5.37%
0.90%	1654.1	1552.2	6.56%	1936.9	1847.7	4.83%	2408.2	2286.7	5.31%
1.35%	1647.8	1549.1	6.37%	1930.1	1833.6	5.26%	2399.9	2282.1	5.16%
1.80%	1641.6	1544.7	6.27%	1923.2	1832.1	4.97%	2391.5	2183.5	9.53%
3.60%	1616.3	1474.2	9.64%	1895.6	1776.1	6.73%	2367.8	1900.9	24.56%
5.40%	1590.7	1374.2	15.75%	1867.5	1738.4	7.43%	2333.5	1818.1	28.35%
9.09%	1538.2	1148.4	33.94%	1809.6	1661.2	8.93%	2262.6	1738.2	30.17%
9.54%	1531.5	1145.7	33.67%	1802.2	1660.6	8.53%	2253.6	1705.5	32.14%
10.91%	1511.3	1074.9	40.60%	1779.8	1192.6	49.24%	2226.1	1663.2	33.84%
16.36%	1427.4	681.75	109.37%	1686.4	1087.9	55.01%	2111.4	1314.0	60.68%

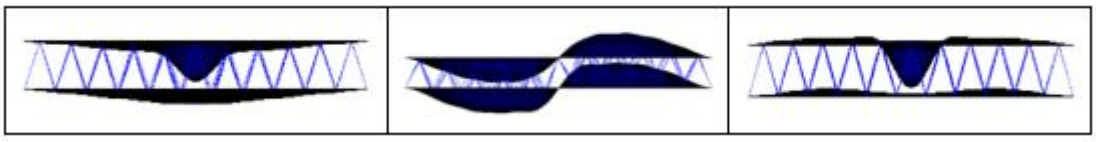

Fig. 2 Vibration of partly moved imperfect lattice sandwich plate

The vibration results for these two imperfection types are listed in Table 3. Compared with the FEM results in Table 3.a, the approximate analytical method can give a good prediction when the missing ratio is between 0.45%~16.36%, where the maximum error is less than 9.0%. For partly moved missing type, the vibration characteristics are complex (Table 3). The FEM results illustrated in Table.3.b show that the prediction method (Eqs. (1)-(7)) cannot reflect the vibration characteristics when the missing ratio is greater than 1.8%. And this is mainly caused by the local vibration mode due to the partly moved area. The

whole vibration mode seems a mixture of local-global vibration interaction (please see Fig.2). In practical, due to the complexity of boundary condition, the precision of analytical model is very difficult to achieve. As an initial estimation, the local vibration mode of missing area can be firstly calculated based on the model of section 3.1.2.

4. Engineering Prediction Model of Structural Deflection and Discussion

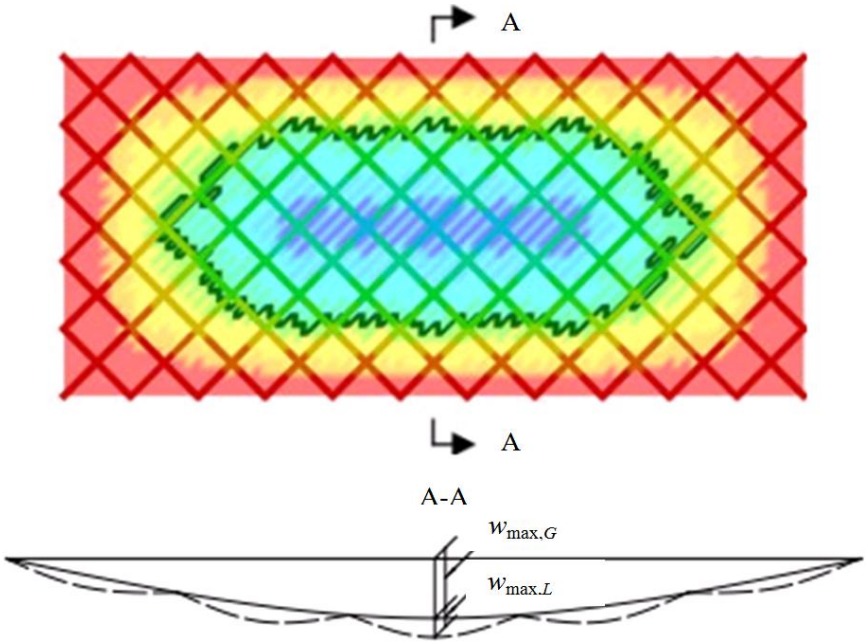

Fig. 3 Deformation characteristics of lattice sandwich plate

In this section, a novel engineering model is performed to investigate the deformation characteristics of ILSP when the structural deformation is in linear region as shown in Fig. 3. The total deformation field can be divided into two components:

(1) The global bending deformation field of ILSP (w_G).

(2) The local bending deformation field of each cell (w_L).

$$w = K_1(t)w_G + K_2(t)w_L \tag{8}$$

where K_1 and K_2 are dynamic coefficient for total and local deformation respectively, when the dynamic effect is considered. And the calculation of dynamic deflection in linear elastic range under uniform impact pressure is given by following equation,

$$K(t) = \frac{w_{dynamic}(t)}{w_{static}} = \frac{\omega}{p_{\max}}\int_0^t p(\tau)\sin[\omega(t-\tau)]d\tau \tag{9}$$

where $K(t)$ is the dynamic inertial effect factor function varied with time, Substitute Eq. (9) into Eq. (8), it has,

$$w = \frac{w_G\omega_G}{p_{\max,G}}\int_0^t p_G(\tau)\sin[\omega_G(t-\tau)]d\tau + \frac{w_L\omega_L}{p_{\max,L}}\int_0^t p_L(\tau)\sin[\omega_L(t-\tau)]d\tau \tag{10}$$

where ω_G is the first circular frequency of global ILSP, ω_L is the first circular frequency of ILSP local cell. ω_G can be calculated from Eqs. (1)-(7). The method of calculation for ω_G can be referred in [43].

In the water entry problem, generally, the compressibility effects can be divided as two parts. The first part of compressibility effects is the compressibility of water, while the second compressibility effect is the compressibility of air respectively. Some previous authors have included the effects of compressibility on the flow during impact [48-50]. The water entry bodies can be divided as three types, which are plate body, blunt body and pointed body. For flat or nearly flat bodies, the hydroelasticity of plate and the compressibility of air cushion should be included. For blunt body, the compressibility of liquid should be included in the first instants as the flow is accelerated from rest. After the fluid particles have reached the velocities associated with the subsonic stage of water entry compressibility can be ignored. As pointed out by Korobkin & Pukhnachov [48-49], there are many difficulties to describe and solve the water entry mathematical model, such as the multiphase, the fluid-solid interaction and the nonlinearity et al. One of these key difficulties is the compressibility of air cushion. To avoid this difficulty, based on the assumption the water impact pressure $p_{\max}$ is the peak impulsive pressure for FSI surface which can be calculated in the following,

$$p_{\max} - p_{\infty} = A v^{B} \tag{11}$$

where p_{∞} is atmosphere pressure, A and B are also the empirical parameters. If the logarithm is used to the Eq. (10) left and right, we can obtain,

$$\ln\left(p_{\max} - p_{\infty}\right) = \ln A + B \ln v \tag{12}$$

We see that the logarithm value of ($p_{\max}$- p_{∞}) is linear with the logarithm value of water entry velocity v. To calculate the water impact $p_{\max}$, the two unknown parameters in the Eq. (12) are A and B. And the parameters A and B can be determined from a least square linear fit based on a few numerical simulations or experiments. The values of A and B are constants though the range of water entry pressure varies widely. It must be pointed out that the coefficients A, B in Eq. (12) are different for the average (whole) FSI pressure and the central FSI pressure, respectively. For example, from our previous study [43], the performance of central FSI pressure for perfect lattice sandwich panels follows a linear trend, as determined from a least square linear fit,

$$\ln\left(p_{\max,L} - p_{\infty}\right) = 4.05 + 1.44 \ln v \tag{13}$$

By means of the least square linear fit, the average (whole) FSI pressure for perfect lattice sandwich panels is also determined,

$$\ln\left(p_{\max,G} - p_{\infty}\right) = 2.63 + 1.69 \ln v \tag{14}$$

The dynamic coefficient K is only associated with the fundamental circular frequency ω and the impact duration time $2\tau_s$. For the average (whole) FSI pressure, a simplified expression to define the impulsive shape $p_G(\tau)$ in Eq. (10) as following [43],

$$p_G(t) = \begin{cases} \lambda_{1,G} t^2 + \lambda_{2,G} t, & 0 \le t \le 2\tau_{s,G} \\ 0, & 2\tau_{s,G} \le t \end{cases} \tag{15}$$

where

$$\lambda_{1,G} = -\frac{p_{\max,G}}{\tau_s^2}, \quad \lambda_{2,G} = \frac{2p_{\max,G}}{\tau_s}, \quad 2\tau_{s,G} \simeq \frac{\left(2.1 \sim 2.6\right)\sqrt{a^2 + b^2}}{C_0} \tag{16}$$

where C_0 is the sound speed of air (C_0= 340 m/s).

Similarly, for local FSI pressure, it has,

$$p_L(t)=\begin{cases}\lambda_{1,L}t^2+\lambda_{2,L}t,\ 0\le t\le 2\tau_{s,L}\\ 0,\qquad\qquad 2\tau_{s,L}\le t\end{cases} \tag{17}$$

where

$$\lambda_{1,L}=-\frac{p_{\max,L}}{\tau_s^2},\quad \lambda_{2,L}=\frac{2p_{\max,L}}{\tau_s},\quad 2\tau_{s,L}\simeq\frac{(2.1\sim 2.6)\sqrt{a^2+b^2}}{C_0} \tag{18}$$

The last two unknown parameters w_G and w_L can be calculated from following,

$$w_G=\frac{4p_{\max,G}a^4}{\pi^4 D_1}\sum_{m=1,3\ldots}^{\infty}\frac{(-1)^{\frac{(m-1)}{2}}}{m^5}\left[\left(1-\frac{\alpha_m th(\alpha_m)+2}{2ch(\alpha_m)}\right)-\delta_m\left(1-\frac{1}{ch(\alpha_m)}\right)\right] \tag{19}$$

$$+\sum_{m=1,3\ldots}^{\infty}(-1)^{\frac{(m-1)}{2}}\left(\frac{\alpha_m th(\alpha_m)}{2m^2\pi^2 ch(\alpha_m)}\frac{a^2}{D_1}H_m\right)+\sum_{n=1,3\ldots}^{\infty}(-1)^{\frac{(n-1)}{2}}\left(\frac{\alpha_n th(\alpha_n)}{2n^2\pi^2 ch(\alpha_n)}\frac{a^2}{\alpha^2 D_1}G_n\right)$$

$$\alpha_m-(\alpha_m th(\alpha_m)-1)th(\alpha_m)+2\delta_m\left(th(\alpha_m)-\frac{m\pi}{\eta_m}th(\alpha_m)\right)H_m \tag{20}$$

$$+\sum_{n=3}^{\infty}\frac{8nm^2}{\alpha}\left[\frac{1}{\alpha^3\pi\left(\frac{m^2}{\alpha^2}+n^2\right)^2}-\frac{\delta_m}{m^2\pi}\left(\frac{1/\alpha}{\frac{m^2}{\alpha^2}+n^2}-\frac{\pi^2}{\alpha\eta_n^2+\frac{m^2\pi^2}{\alpha}}\right)\right]G_n$$

$$+\frac{1}{m^3}\left[(\alpha_m th(\alpha_m)+1)th(\alpha_m)-\alpha_m\right]p_{\max,G}=0$$

$$\alpha_n-(\alpha_n th(\alpha_n)-1)th(\alpha_n)+2\delta_n\left(th(\alpha_n)-\frac{n\pi}{\eta_n}th(\alpha_n)\right)G_n \tag{21}$$

$$+\sum_{n=3}^{\infty}\frac{8mn^2}{\alpha}\left[\frac{1}{\pi\left(\frac{m^2}{\alpha^2}+n^2\right)^2}-\frac{\delta_m}{n^2\pi}\left(\frac{1/\alpha}{\frac{m^2}{\alpha^2}+n^2}-\frac{\pi^2}{\frac{\eta_m^2}{\alpha^2}+n^2\pi^2}\right)\right]H_m$$

$$+\frac{1}{\alpha^2 n^3}\left[(\alpha_n th(\alpha_n)+1)th(\alpha_n)-\alpha_n\right]p_{\max,G}=0$$

$$\alpha_m=\frac{m\pi b}{2a},\ \eta_m=\left[m^2\pi^2+\frac{2}{\delta_a(1-\nu)}\right]^{1/2},\ \delta_a=\frac{D_1}{C_G a^2},\ \delta_m=m^2\pi^2\delta_a \tag{22}$$

$$\alpha_n=\frac{n\pi a}{2b},\ \eta_n=\left[n^2\pi^2+\frac{2}{\delta_b(1-\nu)}\right]^{1/2},\quad \delta_b=\frac{D_1}{C^*_G b^2},\ \delta_n=n^2\pi^2\delta_b \tag{23}$$

$$w_L = 0.005507 \frac{p_{\max,L} d_c^4}{D^*_1} \tag{24}$$

where C^*_G is the equivalent shear stiffness of lattice core, D^*_1 are the bending stiffness of ILSP, w_L is the local maximum deformation, $p_{\max,L}$ is the maximum value of water entry pressure loading on central cells, d_c is the width of cell (see Fig. 1) and D_f is the flexural rigidity of cell face sheet. And the other nomenclatures have the same meanings as mentioned in the previous study.

$$D_f = \frac{E t_f^3}{12\left(1-\nu^{*2}\right)} \tag{25}$$

If the detailed expression of ω_G, ω_L, w_G, w_L, $p_{\max}$, $p(t)$ and $2\tau_s$ are obtained from Eqs. (1)-(25), the value of dynamic coefficient K can be easily obtained. And the maximum value of $K(t)$ at $t = t_0$ is commonly considered, which satisfies the following conditions [43],

$$\frac{dK(t)}{dt} = 0\Big|_{t=t_0}, \frac{d^2K(t)}{dt^2} < 0\Big|_{t=t_0} \tag{26}$$

5. Fluid-Structures Interaction Numerical Simulation

5.1 Numerical Analysis Model

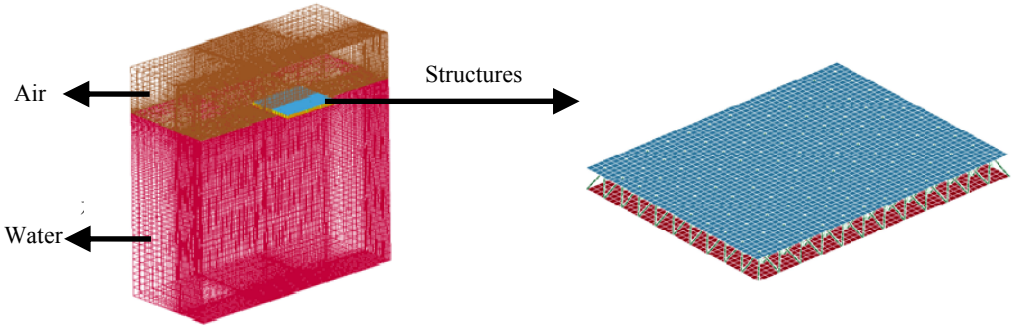

Fig. 4 Numerical simulation model

The top (bottom) face sheet and corrugated core are modeled as a plane plate using 52000 quadrilateral shell elements(shell 163, KEYHOFF formulation, hourglass control, five degrees of freedom per node u_x, u_y, u_z, θ_x, θ_y, finite membrane strains elements, with 5 integration points).The detailed Lagrange FE model of ILSP can be seen in Fig. 4. In the simulation, the Lagrange material of the ILSP is modeled to be S304 steel. In order to consider the strain rate effect, Cowper-Symonds model is adopted. And the material property constants can be referred in [43-44].

To model the fluid inside and outside the ILSP, two Euler domains are used. The outer domain has the ILSP surface (including top face sheet, bottom face sheet and out-off rigid wall) as part of the fluid boundary, Euler material is outside the ILSP surface and there is no material inside the ILSP surface. The contents inside the ILSP are modeled in the inner domain and this domain is also enclosed by the ILSP out surface. Therefore both Euler domains use the ILSP surface as part of their enclosure. Here, the outer boundary of the outer domain is given by a sufficiently large fixed box. Here, pressure at the water Euler domain is set to the hydrostatic pressure by using the *INITIAL_HYDROSTATIC_ALE keyword cards. The Euler mesh contains the water and the air on the top of the water.

The fluid mesh used for this problem are consisted of a block of elements, with the dimensions are 2.5m*2.5m*4.0m. And this fluid block of water and air are meshed with 100*100*90 hexahedron elements, for a total of 900000 fluid elements (Fig. 4). The finest gird size of Euler domain is 0.005 m in this simulation. All the boundary conditions for out fluid mesh are given a "flow" boundary condition by adopting non-reflecting boundary keyword card. In order to model fresh water, a polynomial equation of state was conducted. This state equation (EOS) of fresh water relates the pressure in the fluid to the acoustic condensation μ and the specific internal energy by:

$$P = \begin{cases} a_1\mu + a_2\mu^2 + a_3\mu^3 + \left(b_0 + b_1\mu + b_2\mu^2\right)\rho_0 E_w \left(\mu > 0\right) \\ a_1\mu + \left(b_0 + b_1\mu\right)\rho_0 E\left(\mu < 0\right) \end{cases} \tag{27}$$

where μ= (ρ-ρ_w)/ρ_w , ρ_w is the initial density of fresh water, E_w is the specific internal energy per unit mass, and a_1 , a_2 , a_3 , b_0, b_1 are constants for the fluid. And the upper equation applies to a fluid in a compressed state, while the lower applies to a fluid in an expanded state. The constants for this equation for fresh water are provided in literature [43-44].

The gamma law gas model is adopted for the EOS of air,

$$P = \left(\gamma - 1\right)\rho_a E_a \tag{28}$$

where ρ_a is the density of air, γ is the heat capacities of the gas and E_a is the specific internal energy of air. The initial pressure of air is set to 1.0×10^5 Pa.

In this analysis, the Arbitrary Lagrange-Euler (ALE) Coupling algorithm is used. The Lagrangian and Eulerian meshes are geometrically independent, and interact via coupling surface. The coupling surface 'cuts across' Eulerian elements which contain multi-material air and water, changing their volume and surface areas. As the finite element mesh deforms under the action of the impact pressure from the Eulerian mesh, the resulting FEM deflection then influences subsequent material flow and pressure forces in the Eulerian mesh, resulting in automatic and precise coupling of FSI. In general, it is known that the results based on ALE algorithm are sensitive to the Euler mesh density. So the Euler mesh needs to be fine enough to capture the highest gradients in the pressure fields, yet a coarser mesh is favorable in terms of computational cost. In addition, the selection of the contact stiffness in penalty is based on contact algorithm, it is required the maximum pressures are approximately known ahead. The non-physical contact penetration can be controlled. To verify the reliability of the developed finite element model, compared with experimental results, the water entry analyses of a circular monolithic plate are illustrated in our previous study [19, 43].

5.2 Basic Water Entry Mechanism and Impact Pressure

5.2.1 Basic Water Entry Mechanism

As an illustration, the case of C1' is analyzed here. The entire water entry process can be divided into three stages as follows.

First Stage; Structure begins to drop → Air compression begins;

Second Stage; Air compression begins → Structure begins to contact water;

Third Stage; Structure begins to contact water → Structure immerses in water.

In this case, the duration predicted by numerical simulation $2\tau_s$=11.5 ms coincides with the empirical estimations ($2\tau_s$=10.7ms) from Eqs. (11)-(12). The contacting water time t observed by the numerical simulation is ~19.0ms. The result from the simulation shows that when t >25.0ms, the water jet begins to split into two parts as plotted Fig.7. Furthermore, the shape of the water entry jet calculated by the ALE coupling algorithm cannot capture the spatter of the droplets. From the authors' view, this phenomenon is probably caused by the

instability of fluid flow. Some small perturbations may be from some uncontrollable practical factors, such as the minor asymmetries in the simulation.

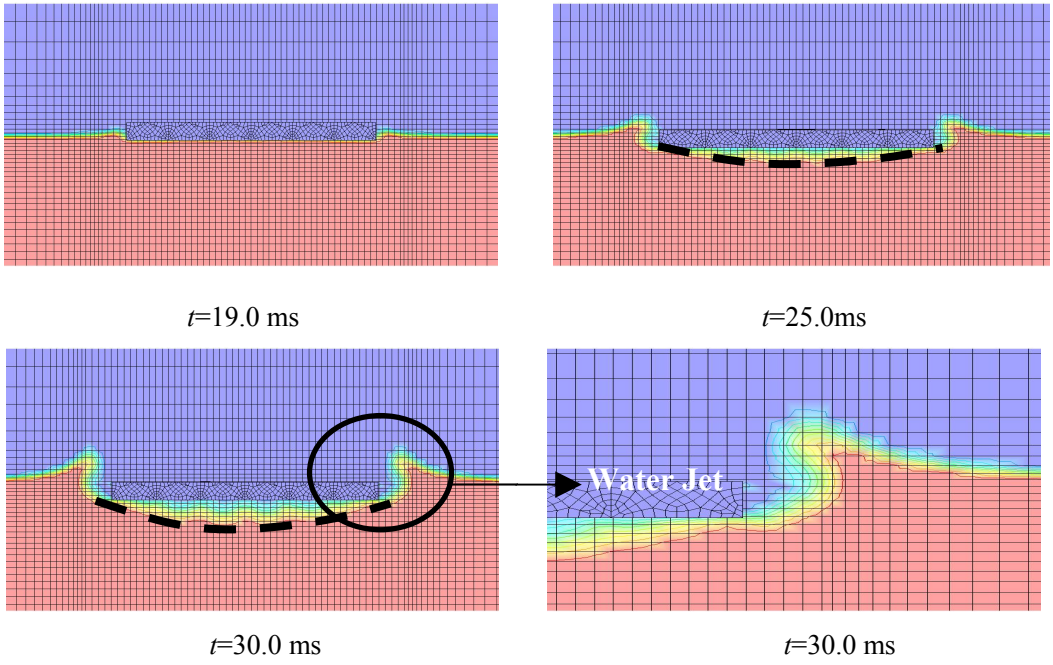

t=19.0 ms *t*=25.0ms

t=30.0 ms *t*=30.0 ms

Fig. 5 The basic water entry process of ILSP

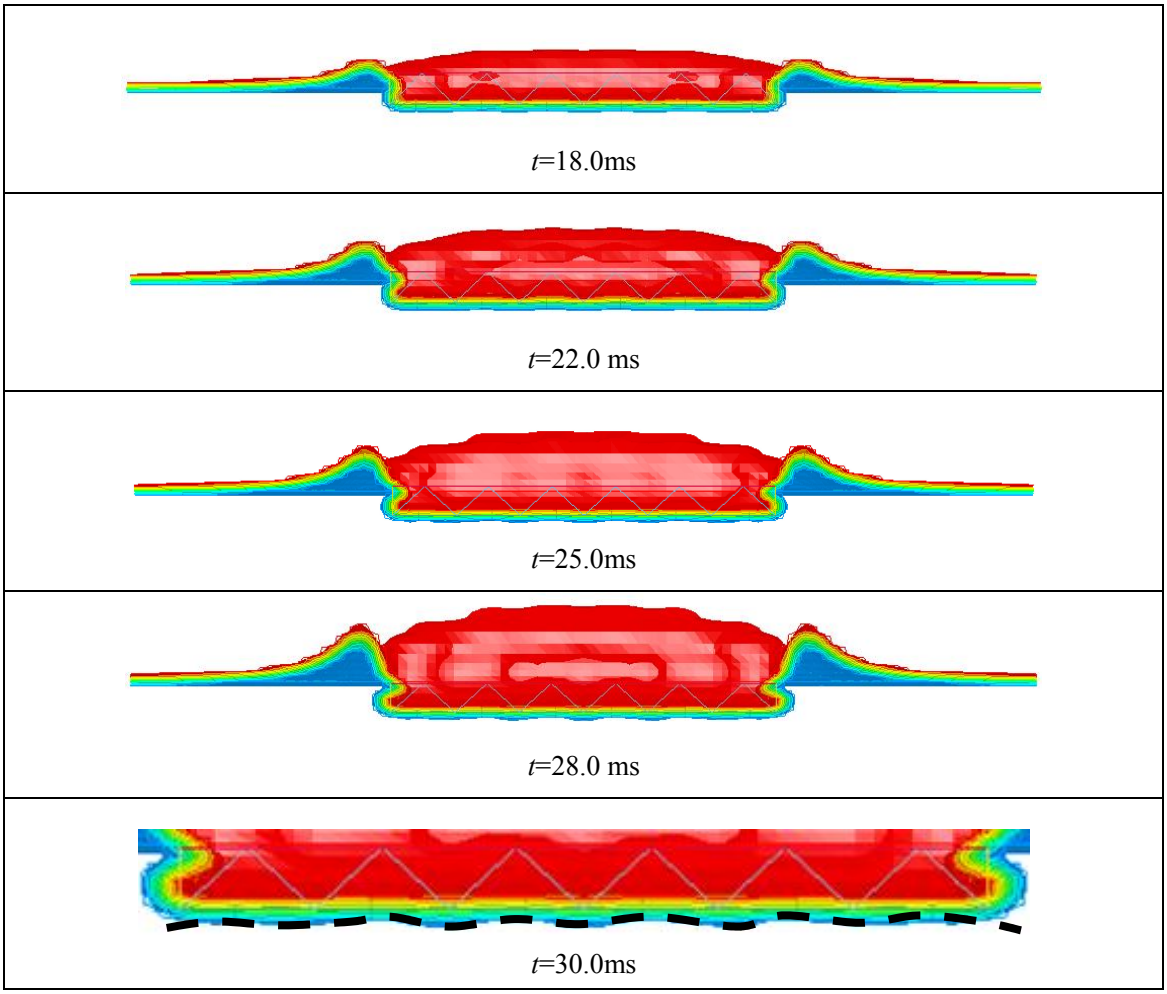

t=18.0ms

t=22.0 ms

t=25.0ms

t=28.0 ms

t=30.0ms

Fig. 6 Volume distribution isosurface of water entry process

From the simulation results, it is obtained that the global air cushion is significant from Fig. 5 (please see the black dash line). Due to the global elastic deformation, the shape of this air cushion is not rectangular. And the fluid materials volume distribution isosurface also shows the local air cushion exists during the initial water entry duration (Fig. 6). This local cushion is caused by lattice cell local deformation which has significant effects on the water entry pressure and dynamic responses of ILSP. Because of the existence of this local air cushion, which plays a role as a buffer device, the peak value of average FSI pressure of contacted-water wet face sheet is lower than that of monolithic plate which has been certificated in our previous study [43-44].

As the effects of local air cushion, the local hydroelasticity is important in the dynamic responses of ILSP. Due to the local loading, the high frequency responses of pressure are also induced as shown later in the pressure-time history curve (please see in Fig. 8). And this local high frequency response is more significant if the loss imperfection is more seriously (please see in Fig. 9). So, the whole response of ILSP is the combination of the multiple global deformations, the lattice cell local deformations, the air cushion and the free surface interaction. Furthermore, some other strong nonlinear phenomenon such as flow turbulence and multiphase flow mixture *et al*. phenomenon may be also exists which cannot captured by present analytical solution and numerical simulation. And it must be studied by future more finely experimental measurement of micro-scale flow structures in FSI surface.

5.2.2 Impact Pressure Results for $2\tau_5 f_s$~5 (the hydroelastic effect is not significant)

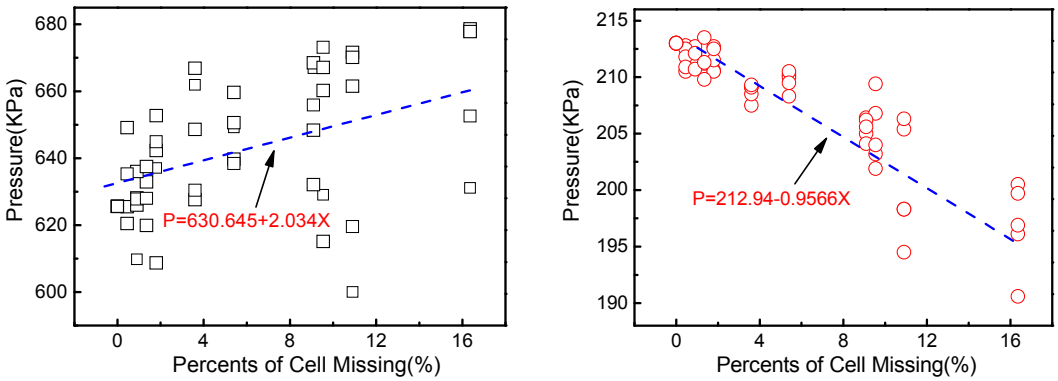

(a) Relation between missing percentage and water entry pressure for RM-ILSP (left: central, right: whole FSI surface)

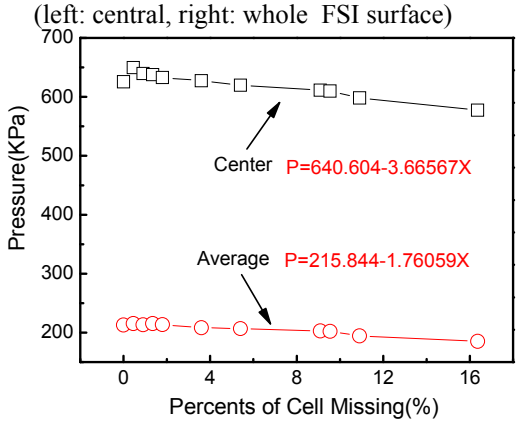

(b) Relation between missing percentage and water entry pressure for PM-ILSP

Fig. 7 Relation between missing percentage and water entry pressure ($2\tau_5 f_s$~5)

The relation between core truss missing ratio and water entry pressure is shown in Fig. 7 for RM-ILSP and PM-ILSP when water entry velocity is 5m/s. According to the results as plotted in Fig. 7, by means of the least square fit, the following observations can be drawn.

For RM-ILSP:

$$P_{imperfect} = P_{perfect}\left(1 + 0.31\eta\right) \qquad for\ center \tag{29}$$

$$P_{imperfect} = P_{perfect}\left(1 - 0.45\eta\right) \qquad for\ whole\ \text{FSI}\ Surface \tag{30}$$

For PM-ILSP:

$$P_{imperfect} = P_{perfect}\left(1 - 0.57\eta\right) \qquad for\ center \tag{31}$$

$$P_{imperfect} = P_{perfect}\left(1 - 0.81\eta\right) \qquad for\ whole\ \ \text{FSI}\ Surface \tag{32}$$

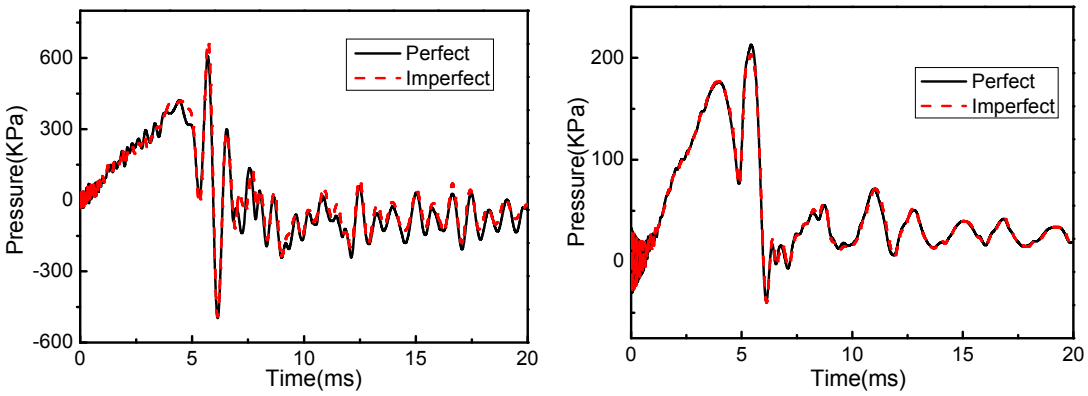

Fig. 8 Comparison of perfect and imperfect water entry pressure curves for RM-ILSP (left: central, right: whole FSI surface) ($2\tau_s f_s$~5)

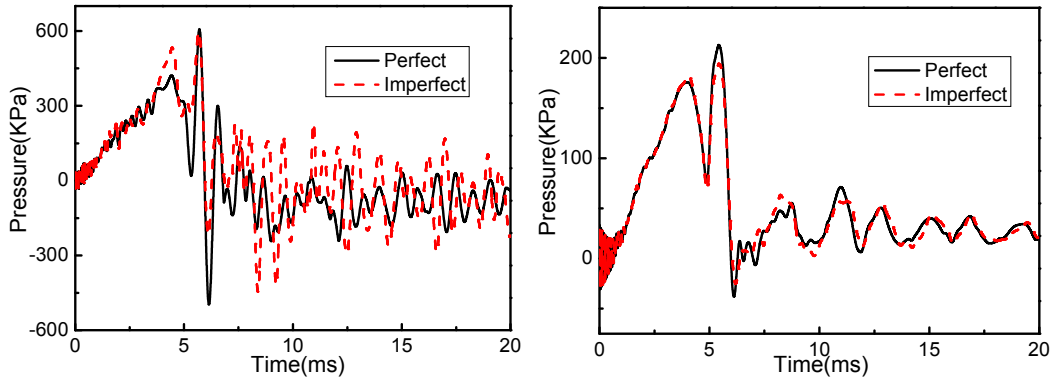

Fig. 9 Comparison of perfect and imperfect water entry pressure curves for PM-ILSP (left: central, right: whole FSI surface) ($2\tau_s f_s$~5)

The local FSI pressure at the center point increases slowly (<4%) when the missing ration varies from 0.45% to 16.36%. But the water entry pressure of total FSI surface for RM-ILSP decreases linearly with fraction of missing trusses, with a roughly 4.5% (from 212KPa to 195KPa) respectively in pressure for every 10% reduction in relative density. This is mainly because the core of RM-ILSP becomes softer when E^*, G^* are smaller. Compared with the Eq. (29) and Eq. (31), it shows that the changing trend of missing ratio is different between RM-ILSP and PM-ILSP. This phenomenon reveals that the random missing truss could change the space distribution of water entry pressure. And the local area of RM-ILSP may be becoming 'harder'. This conclusion also certificated from Fig.7 (a) which shows the discrete pressure value of central point. And the maximum difference between the lower point and upper point value is about 80KPa (~15%). This gives a conclusion that the core topology

structure is very important in the FSI. The least square fit data also illustrate that the decrease changing trend of PM-ILSP is faster than that of RM-ILSP. Compared with Fig. 8 (a) and Fig. 9 (a), the pressure-time curve shows that the oscillation amplitude of PM-ILSP is greater in the whole water entry process. The same conclusion of total FSI pressure also can be summarized from Fig. 8 (b) and Fig. 9 (b).

5.2.3 Impact Pressure Results for $2\tau_s f_s$~1.0 (the hydroelastic effect is significant)

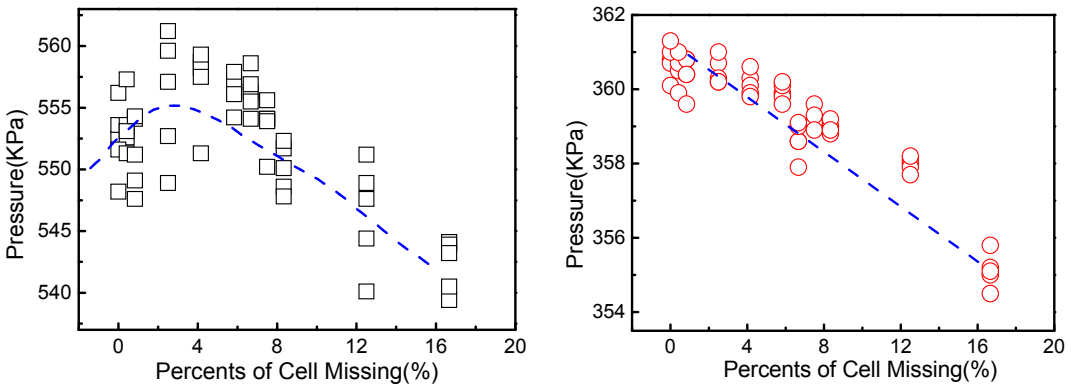

(a) Relation between missing percentage and water entry pressure for RM-ILSP (left: central, right: whole FSI surface)

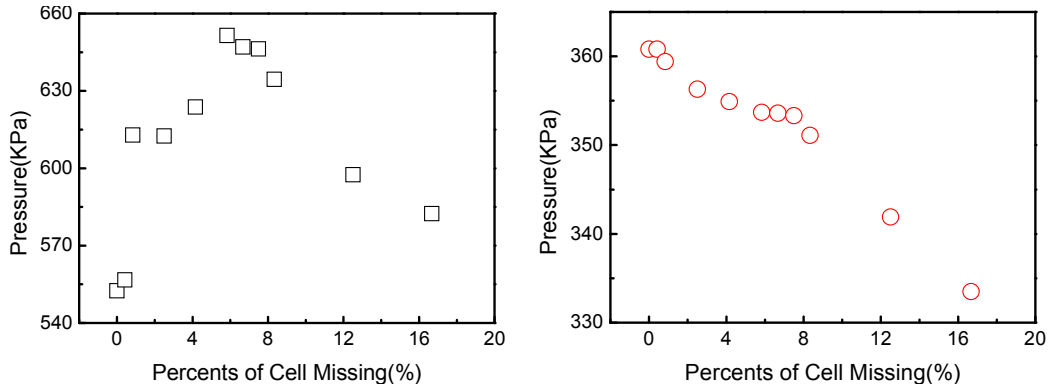

(b) Relation between missing percentage and water entry pressure for PM-ILSP (left: central, right: whole FSI surface)

Fig. 10 Relation between missing percentage and water entry pressure ($2\tau_s f_s$~1)

For RM-ILSP:

$$P_{imperfect} \cong P_{perfect} \qquad for\ center \tag{33}$$

$$P_{imperfect} = P_{perfect}\left(1 - 0.221\eta\right) \qquad for\ whole\ \text{FSI}\ Surface \tag{34}$$

For PM-ILSP:

$$P_{imperfect} \simeq P_{perfect} \qquad for\ center \tag{35}$$

$$P_{imperfect} = P_{perfect}\left(1 - 0.638\eta\right) \qquad for\ whole\ \text{FSI}\ Surface \tag{36}$$

When the hydroelastic effect is significant, the numerical simulation results reveal that the random missing imperfection effect on the dynamic response of RM-ILSP is complex as shown in Fig. 10 (a). When the missing percentage η is less than 5%, the local FSI water entry pressure seems rise up. But when η>5%, the local FSI pressure is becoming lower while this oscillation amplitude is minor. The same phenomenon also can be found in the response of PM-ILSP. According to the numerical results in Fig. 10 (b), the changing trend is decreasing

about 9.8% for whole FSI surface when η=16%. Compared with Figs. 10 (a) and (b) (here, also compared with Eqs. (34) and (36)), an approximate linear decreasing relation between missing rate and pressure value can be given.

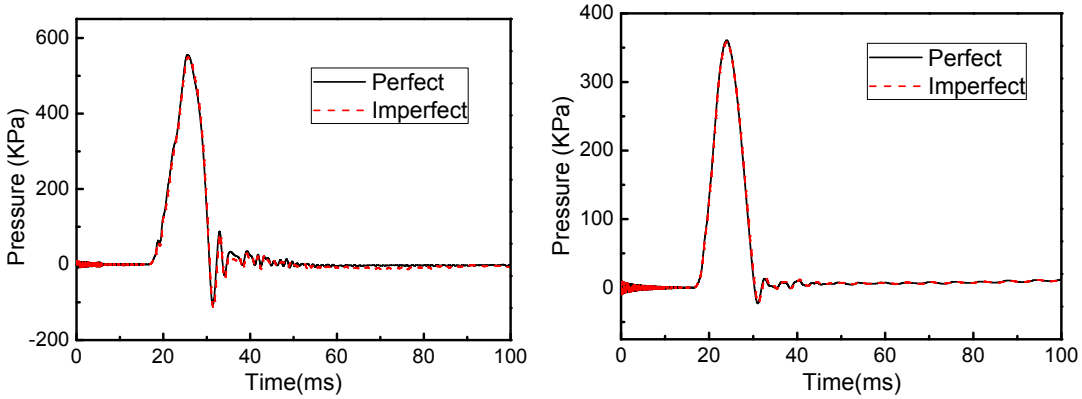

Fig. 11 Comparison of perfect and imperfect water entry pressure curves for RM-ILSP (left: central, right: whole FSI surface) ($2\tau_s f_s$~1)

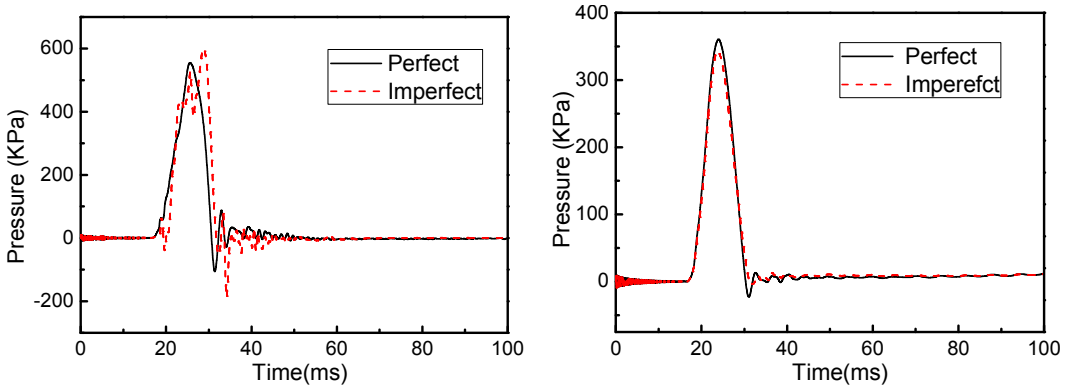

Fig. 12 Comparison of perfect and imperfect water entry pressure curves for PM-ILSP (left: central, right: whole FSI surface) ($2\tau_s f_s$~1)

In Fig. 11 and Fig. 12, the water entry pressure time history curves are given for local coordinate and whole surface. Compared the water entry curves detailed, the random missing imperfection also has little effect on dynamic response. But the effect of local partly missing imperfection is more significant (Fig. 12). Compared with Fig. 9 and Fig. 12, both for local central point pressure and total FSI surface pressure, the smoothness of pressure curve is more significant when $2\tau_s f_s$~1.0. This may the high frequency pressure response components would be excited by smaller core cell.

5.3 Structural Deflection Response of ILSP

5.3.1 $2\tau_s f_s$~5 (the hydroelastic effect is not significant)

For RM-ILSP, compared with FSI simulation results, with water entry speed v=5m/s, the maximum deformations by using above FE analysis model are illustrated in Fig. 13. It is clear that the changing trend of simulation result is consistent well with theoretical predictions when the reduction of relative density is lower than 10~11%. But the error of this analytical method is greater than 15% when the missing percentage is greater than 12%. This is mainly because the precision of first homogenization approximation in Eq. (4) is not precise enough when the reduction of relative density becomes sufficiently high. Another reason is probably the local deflection of imperfection cell. For PM-ILSP, a detailed comparison analysis in Fig.

13 shows that the maximum deflection has a rapid increase when η=9-10%. Thus, this result indicates that there exists a critical missing ratio point.

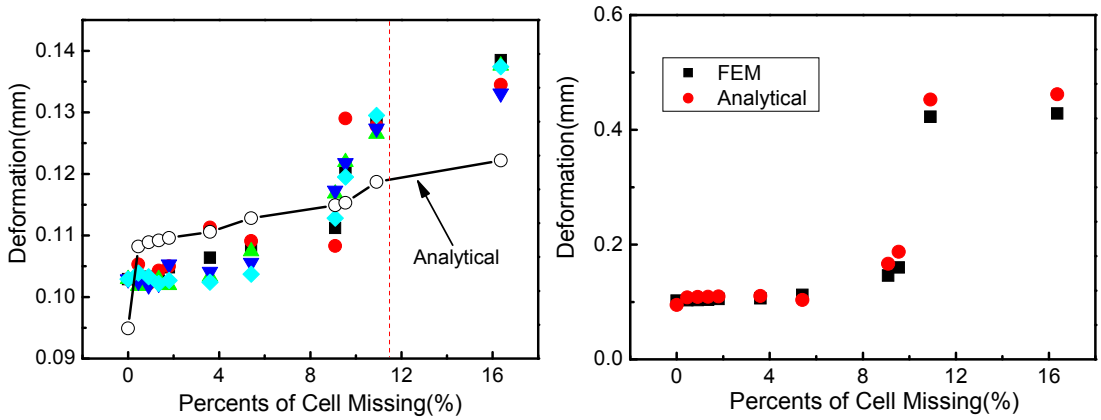

Fig. 13 Relation between missing percentage and water entry pressure ($2\tau_s f_s$~5)

(Left: RM-ILSP, right: PM-ILSP)

5.3.2 $2\tau_s f_s$~1.0 (the hydroelastic effect is significant)

As shown in Fig. 14, the critical deformation point also exits when hydroelastic effect is significant both for RM-ILSP and PM-ILSP. For RM-ILSP, the critical point is nearly equal to 12%. But for PM-ILSP, the critical point is nearly equal to 2%. The computational results reveal that the maximum deformation is increasing very fast (~300%) for PM-ILSP when the missing percentage is about 1%. This means the maximum deformation is insensitive with imperfection ratio. Compared with Fig.13 and Fig. 14, the different critical deformation point exists when hydroelasticity indicator $2\tau_s f_s$ is different. For RM-ILSP cases, the critical deformation point of $2\tau_s f_s$~1.0 (about 12%) is very close to that of $2\tau_s f_s$~5.0 (about 10~11%). But for PM-ILSP cases, the critical point between $2\tau_s f_s$~1.0 (about 2%) and $2\tau_s f_s$~5.0 (about 10~11%) is very variable. This may the effects of different missing trusses region.

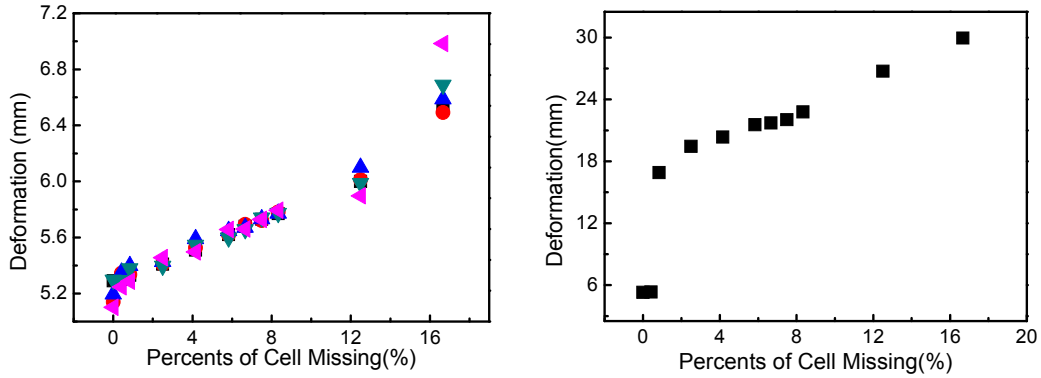

Fig. 14 Relation between missing percentage and water entry pressure

($2\tau_s f_s$~1) (Left: RM-ILSP, right: PM-ILSP)

6. Geometric Parameters Effects Study

When the hydroelastic effect is not significant ($2\tau_s f_s$~5), the effects of parameters can be referred our previous investigation [44]. Thus, only $2\tau_s f_s$~1 is considered here. Both for RM-ILSP and PM-ILSP, three parameters including the face sheet thickness t_b (t_f), the height H_c and the section cross area t_c*t_c are considered here.

6.1 The face sheet thickness t_b (t_f)

For RM-ILSP, as plotted in Fig. 15, when the top face sheet thickness t_f varies from 0.5mm to 5.5mm, the central FSI pressure P_c rises about 11% even η=12.50%. Furthermore, when t_f is greater than 0.5mm, the P_c is nearly about 550KPa. The whole FSI surface pressure P_w rises about 12% 0.5 t_f<1.5mm. But when t_f>1.5mm, the P_w~370KPa. Moreover, when t_f changes, the characteristic of maximum deformation is given in Fig. 16. When t_f varies from 0.5mm to 5.5mm, the deformation value becomes lower dramatically as the bending stiffness increases fast. Particularly, this trend is not significant when t_f >2.5mm. Compared with t_f, the effect of t_b is significant (Fig. 17). As plotted in Fig. 17, P_c increases fast when t_f <2.5mm while this trend is becoming slow if t_f >2.5mm. Thus, the maximum deformation decrease fast when t_f <2.5m (Fig. 18). The effects of face sheet thickness t_b (t_f) for perfect lattice sandwich panel has been investigated by many previous scholars in other field such as bending, vibration and blast *et al* [38-41], some similar conclusions have been given.

For PM-ILSP, if η=12.50%, the central FSI pressure rises P_c about 3% when the top face sheet thickness t_f varies from 0.5mm to 5.5mm, while the FSI pressure P_c increases 5%. That means the change of t_f has little effect on the water entry pressure. And this trend also exits in the analysis of deformation. This is mainly because the majority of deformation is local deformation for water contacted surface. Though the bending stiffness increases fast, the global deformation has little effect on whole deformation. Compared with Fig. 16 and Fig. 19, the effect of t_f is more significant for RM-ILSP cases. We think this may the average of random missing plays a key role in the response which makes ILSP core softer. While the central effect of local missing is more important for PM-ILSP cases.

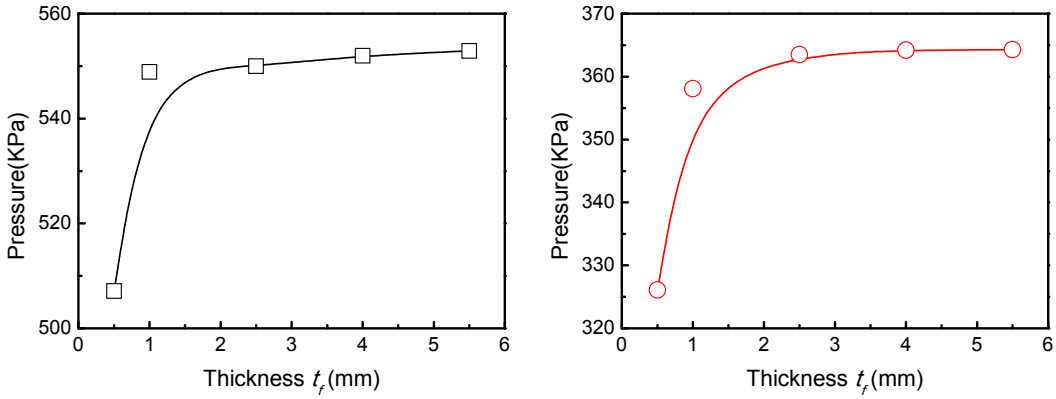

Fig. 15 Effect of t_f on water entry pressure (left: P_c, right: P_w), RM-ILSP

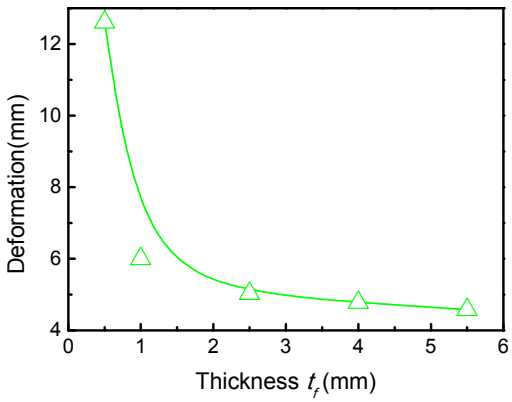

Fig. 16 Effect of t_f on maximum deformation, RM-ILSP

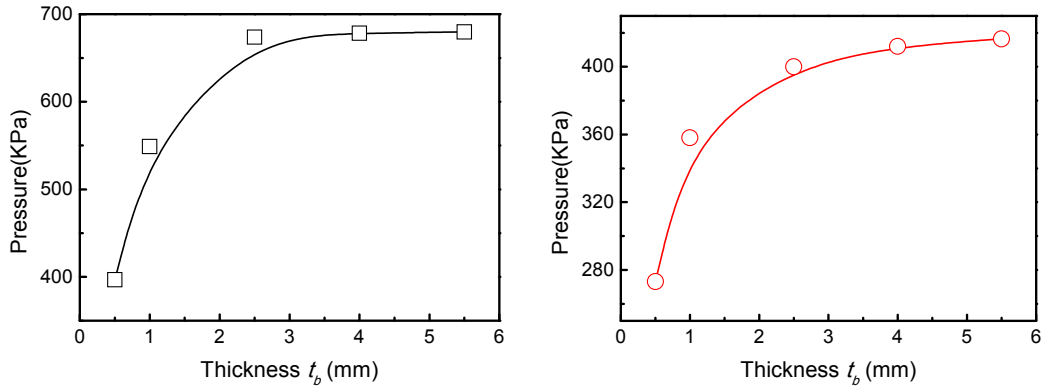

Fig. 17 Effect of t_b on water entry pressure (left: P_c, right: P_w), RM-ILSP

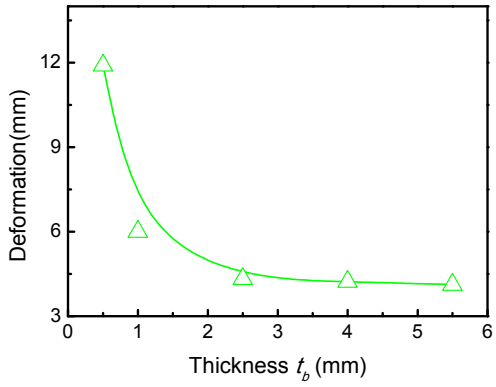

Fig. 18 Effect of t_b on maximum deformation, RM-ILSP

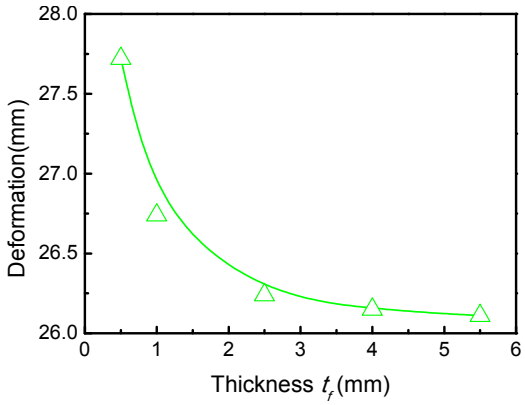

Fig. 19 Effect of t_f on maximum deformation, PM-ILSP

6.2 The core height H_c

For RM-ILSP, H_c has significant effect on the dynamic behavior. As shown in Fig. 20, the water entry FSI pressure is decreasing about 40% when H_c increases from 70.00 to 110.00mm. And the changes for the deformation of ILSP is dramatically (Fig. 21) from 50.0 mm to 5.0 mm. But this trend becomes slow when H_c>90.0 mm. This can be interpreted as the local buckling phenomenon occurs when the H_c is relative high. Compared with Fig. 20(a) and Fig. 20(b), the decreasing ratio of central pressure value and total FSI pressure value is nearly the same (~30%). The minimum deflection critical point in Fig. 21 shows that the optimization is needed in the parameter design of ILSP. Moreover, it shows that the effects of H_c on the changing trend of water entry pressure is more dramatically than that of t_b(t_f). And the conclusion is also suited for the effects of defection characteristics.

For PM-ILSP, the changing trend of dynamic behavior curve is similar with RM-ILSP. When 20.0 mm<H_c<40.0 mm, the water entry pressure decreasing trend is more dramatically

(nearly ~50%) as shown in Fig. 22. Furthermore, the changing trend seems more complex when 40.0 mm<H_c<60.0 mm. We think the basic reason for this phenomenon is may be the changing of pressure spatial distribution. For the characteristics deformation of PM-ILSP, we find it decreases dramatically when H_c<90.0mm (Fig. 23). This may be caused by two reasons. The first is the deceasing of water entry pressure; the second is the increasing of bending stiffness. Compared with Fig. 21 and Fig. 23, it seems minimum deflection critical point is not existed for PM-ILSP.

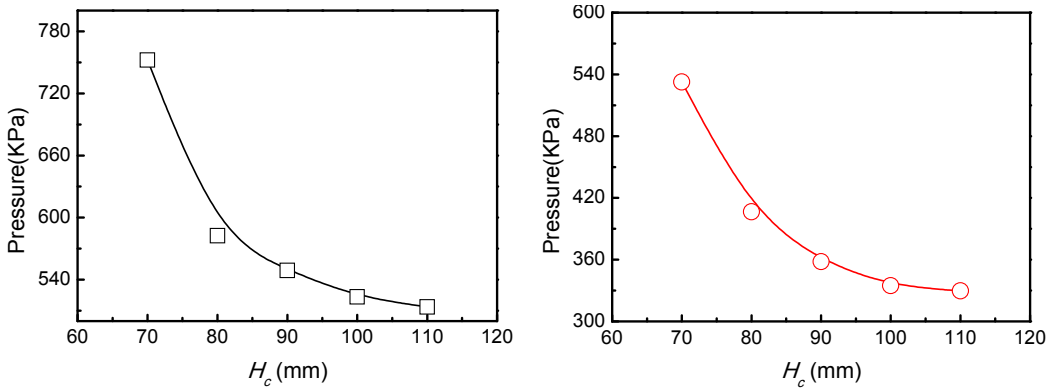

Fig. 20 Effect of H_c on water entry pressure (left: P_c, right: P_w), RM-ILSP

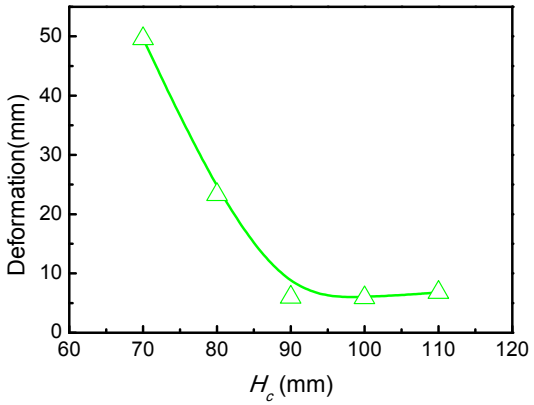

Fig. 21 Effect of H_c on maximum deformation, RM-ILSP

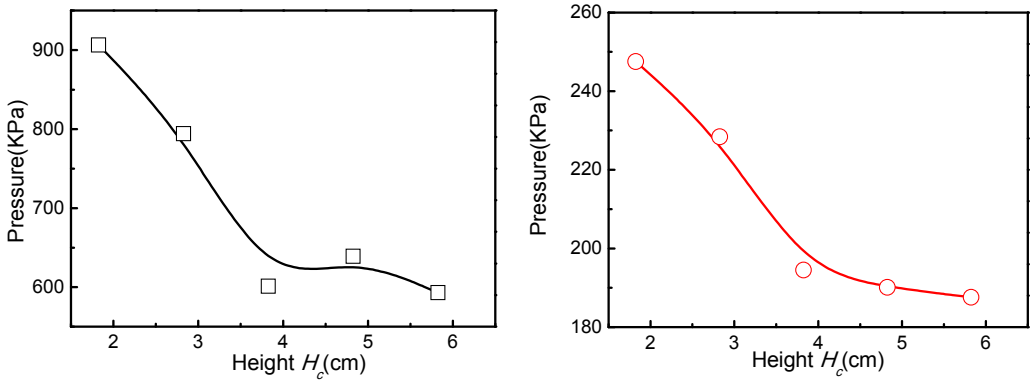

Fig. 22 Effect of H_c on water entry pressure (left: P_c, right: P_w), PM-ILSP

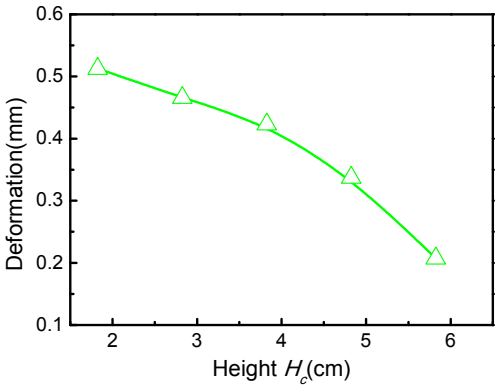

Fig. 23 Effect of H_c on maximum deformation, PM-ILSP

6.3 The section cross area t_c*t_c

For random moved ILSP, the last parameter is the section cross area t_c*t_c. According to the numerical simulation results, the changing characteristic is rather different when t_c increases from 5.0mm to 7.0mm. As shown in Fig. 24, the central water entry pressure P_c is decreasing fast when t_c<6.0mm. But the changing trend is becoming increasing when t_c>6.0mm. This means the water entry pressure also has a critical point when t_c changes. This may be caused by the non-uniform distribution of water entry pressure due to local stiffened truss. For global FSI pressure P_w, the changing trend of is increasing fast when t_c>6.5mm. This increasing trend is slow when t_c<4.5mm. Compared in Fig. 24, the changing trend between P_c and P_w is different. As we known, the pressure P_c is a local indicator of pressure distribution; while the pressure P_w is a global indicator of pressure distribution. The structural deformation of ILSP is also sensitive when t_c is changing. As shown in Fig. 25, the maximum deformation is decreasing fast when t_c changes from 2.5mm to 6.5mm. From the numerical simulation, the local truss buckling occurs when t_c is about equal to 2.5mm.

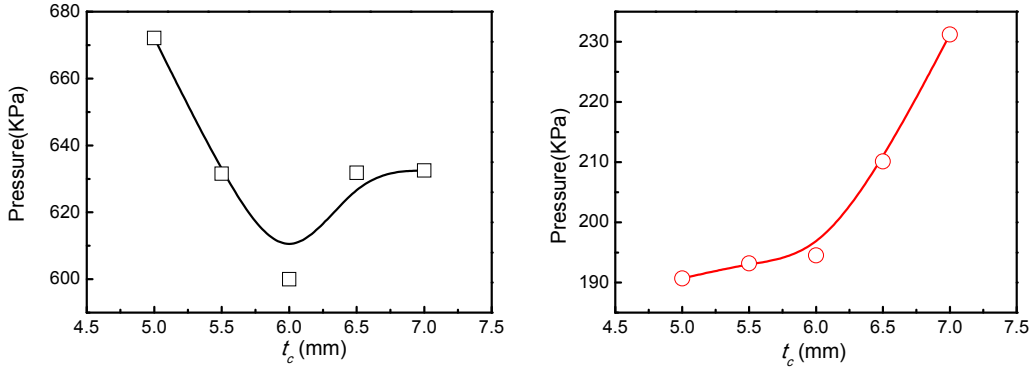

Fig. 24 Effect of t_c on water entry pressure (left: P_c, right: P_w) , RM-ILSP

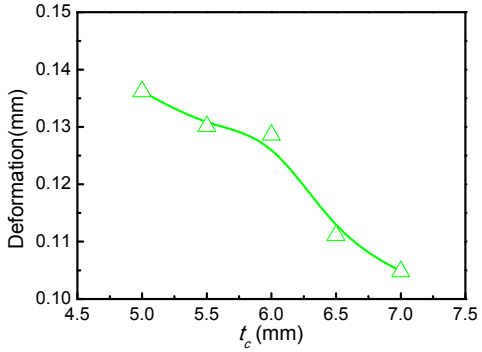

Fig. 25 Effect of t_c on maximum deformation-Random missing

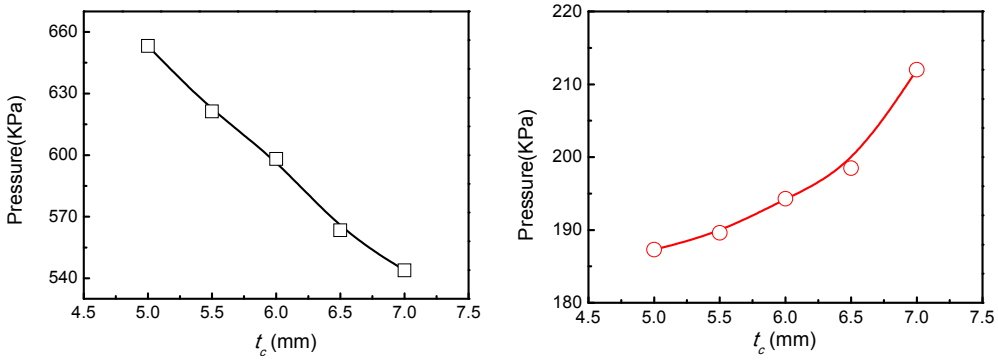

Fig. 26 Effect of t_c on water entry pressure (left: P_c, right: P_w), PM-ILSP

For PM-ILSP, compared with Fig. 24 and 26, the changing trend of water entry pressure for central point is different with that of RM-ILSP. For the central pressure P_c, the water entry pressure is decreasing slowly from 650KPa to 540KPa. But the P_w is increasing about 30KPa (Fig. 26). Compared with the effect of H_c, it shows that the effect of t_c*t_c is minor. Thus, in the parameter design of ILSP, the section area can be seen as a secondary consideration. As plotted in Fig. 27, the changing trend of deformation curve also concludes that the t_c has effect on the dynamic response of PM-ILSP, which is similar with that of RM-ILSP. The central deformation of PM-ILSP is decreasing about 10% when t_c is increasing from 5.0mm to 7.0mm.

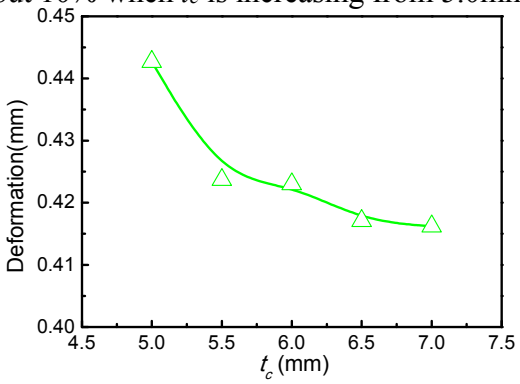

Fig. 27 Effect of t_c on maximum deformation-Partly moved missing

7. Conclusion

In this study, the hydroelastic behavior of lattice sandwich panels with imperfection (ILSP) subjected to water entry is investigated both analytically and numerically. A novel engineering estimation method is proposed to calculate the dynamic response characteristics of ILSP. The FSI numerical model is presented to obtain the detailed water entry behavior for ILSP. To identify the effect of missing ratio on the water entry characteristics, various imperfection scenarios are simulated. Finally, the effects of key parameters such as the face sheet thickness, core height and section of core truss are discussed. This study provides an engineering method for water entry problem of sandwich panels how hydroelastic pressure and maximum structural deformation are affected by the missing imperfection during the manufacture. And the following conclusions could be drawn from the semi-analytical method and numerical simulation results.

(1) When the hydroelastic effect is not significant ($2\tau_s f_s$~5), the random missing imperfection has little effect on water entry pressure of local central point if the missing percentage varies from 0.45%-16.36%; though a more significant effect on the whole water

entry pressure. When the core of ILSP becomes softer, the water entry pressure of central point will decrease by about 10%.

(2) When the hydroelastic effect is significant ($2\tau_S f_s$~1), the random missing imperfection also has little effect on water entry pressure of local central point if the missing ration is varied from 0.45%-16.36%. With the increasing of missing percentages, the water entry pressure decreases. An oscillation phenomenon is identified in the water entry pressure curve. And the water entry pressure of central point decreases about 6.4% when the missing percentage is 16.36%.

(3) The results obtained by engineering estimation model agree well with that of numerical simulation when the imperfection type is random missing and the missing percentage is lower than 12%. But if the missing percentage is greater than 12%, the error becomes larger. And this is mainly caused by the first order approximation in the assumption.

(4) A very interesting phenomenon is that a critical missing percentage exists both for random missing and partly moved imperfection types. If the missing percentage is greater than the critical one, the maximum deformation increases dramatically. Thus, in the engineering practice, the missing percentage must be limited in the critical region which must be emphasized.

(5) The parametric study results show that the thickness of water contacted face sheet, the core height and the section of core truss has significant effect on the water entry response characteristics. If the core truss buckling occurs in the water entry process, this effect is more significant. On the contrary, the top face sheet has neglected effect on the response of ILSP.

Acknowledgement

The authors are pleased to acknowledge the financial support of the National Natural Science Foundation of P.R. China (Contract No. 51079058, 51279065) and Basic Defense Research Program (Contract No. JCKY201606C003).

REFERENCES

[1] Karman, VT. 1929. The impact on seaplane floats during landing. Technical Note No.32, NACA.

[2] Wagner, H. 1932. Phenomena associated with impacts and sliding on liquid surfaces. ZAMM, 12, 4, 193-215. https://doi.org/10.1002/zamm.19320120402.

[3] Kapsenberg, GK. 2011. Slamming of ships: where are we now?. Philosophical Transactions of the Royal Society of London Series A-Mathematical Physical and Engineering Sciences, 369, 2892–2919. https://doi.org/10.1098/rsta.2011.0118.

[4] Faltinsen, OM. 2007. Challenges in hydrodynamics of ships and ocean structures. Brodogradnja/ Shipbuilding: Theory and Practice of Naval Architecture, Marine Engineering and Ocean Engineering, 58, 3, 268-277.

[5] Faltinsen, OM. 2000. Hydroelastic slamming. Journal of Marine Science and Technology, 5, 49–65. https://doi.org/10.1007/s007730070011.

[6] Morabito MG. 2014. Empirical equations for planning hull bottom pressures. Journal of Ship research, 58 (4), 185-200. https://doi.org/10.5957/JOSR.58.4.140006.

[7] Korobkin, AA. 1996. Water impact problems in ship hydrodynamics. In: M. Ohkusu (Ed.), Advances in marine hydrodynamics, Chap 7. Computational Mechanics Publications, Southampton, 323-371.

[8] Korobkin AA., Parau EI., Vanden-Broeck JM. 2011. The mathematical challenges and modeling of hydroelasticity. Philosophical Transactions of the Royal Society of London Series A-Mathematical Physical and Engineering Sciences, 369 (1947), 2803-2812. https://doi.org/10.1098/rsta.2011.0116.

[9] Abrate, S. 2011. Hull slamming. Applied Mechanics Reviews, 64, 6, 1-35.
https://doi.org/10.1115/1.4023571.

[10] Teselkin, DA., Tormakhov, AY. 1988. Numerical and experimental investigation of the entry of a flat plate into water. Fluid Mechanics-Soviet Research, 17, 109-120.

[11] Cointe, R., Armand, JL. 1987. Hydrodynamic impact analysis of a cylinder. Journal of Offshore Mechanics and Arctic Engineering, 109, 3, 237–243. https://doi.org/10.1115/1.3257015.

[12] Matthew, EM. 2006. Characterization of water impact splashdown event of space shuttle solid rocket booster using LS-DYNA. 7th International LS-DYNA User Conference, 266-272.

[13] Jin, SC., Jang, BS., Yim, KH., *et al*. 2016. A study on slamming pressure on a flat stiffened plate considering fluid–structure interaction, Journal of Marine Science and Technology, 21, 309-324. https://doi.org/10.1007/s00773-015-0353-y.

[14] Ng, CO., Kot, SC. 1992. Computations of water impact on a two-dimensional flat-bottomed body with a volume-of-fluid method. Ocean Engineering, 19, 4, 377-393.
https://doi.org/10.1016/0029-8018(92)90036-4 .

[15] Kleefsman, KMT., Fekken, GA., Veldman, EP. *et al*. 2005. A volume-of-fluid based simulation method for wave impact problems. Journal of Computational Physics, 206, 363-393.
https://doi.org/10.1016/j.jcp.2004.12.007.

[16] Shademani, R., Ghadimi, P. 2016. Estimation of water entry forces, spray parameters and secondary impact of fixed width wedges at extreme angles using finite element based finite volume and volume of fluid methods. Brodogradnja/Shipbuilding: Theory and Practice of Naval Architecture, Marine Engineering and Ocean Engineering, 67, 1, 101-124.

[17] Vandamme, J., Zou, QD. 2011. Modeling Floating Object Entry and Exit Using Smoothed Particle Hydrodynamics. Journal of Waterway, Port, Coastal, and Ocean Engineering, 137, 5, 213-224.
https://doi.org/10.1061/(asce)ww.1943-5460.0000086.

[18] Gui, Q., Shao, S., Dong, P. 2014. Wave impact simulations by an improved ISPH model. Journal of Waterway, Port, Coastal, and Ocean Engineering, 140, 3, 005. https://doi.org/10.1061/(ASCE)WW.1943-5460.0000239.

[19] Ando, Y., Fujita, Y., Yamaguchi, I. 1951. On the impulsive force of flat plate falling. Bulletin of Japan Society of Naval Architects and Ocean Engineers, 90, 69-75.
https://doi.org/10.2534/jjasnaoe1952.1956.69.

[20] Chuang, SL. 1966. Experiments on flat-bottom slamming. Journal of Ship Research. 10, 10-17.

[21] Chuang, SL. 1970. Investigation of impact of rigid and elastic bodies with water. NSRDC Report 3248.

[22] Sun, SY., Sun, SL., Wu, GX. 2015. Oblique water entry of a wedge into waves with gravity effect. Journal of Fluids and Structures, 52, 49-64. https://doi.org/10.1016/j.jfluidstructs.2014.09.011.

[23] Yang, XB., Xu, GD. 2018. Numerical simulation of the oblique water entry of wedges with vortex shedding. Brodogradnja/Shipbuilding: Theory and Practice of Naval Architecture, Marine Engineering and Ocean Engineering, 69, 4, 69-83. https://doi.org/10.21278/brod69406.

[24] Marie, SY. 2014. Oblique water entry of a three dimensional body. International Journal of Naval Architecture and Ocean Engineering, 6, 4, 1197-1208. https://doi.org/10.2478/IJNAOE-2013-0239.

[25] Truscott, T., Alexandra, HT. 2009. Water entry of spinning spheres. Journal of Fluid Mechanics, 625, 135-165. https://doi.org/10.1017/S0022112008005533.

[26] Korkmaz, FC., Güzel, B. 2017. Water entry of cylinders and spheres under hydrophobic effects; Case for advancing deadrise angles. Ocean Engineering, 129, 240-252.
https://doi.org/10.1016/j.oceaneng.2016.11.021.

[27] Javanmardi, N., Ghadimi, P., Tavakoli, S. 2018. Probing into the effects of cavitation on hydrodynamic characteristics of surface piercing propellers through numerical modeling of oblique water entry of a thin wedge. Brodogradnja/Shipbuilding: Theory and Practice of Naval Architecture, Marine Engineering and Ocean Engineering, 69, 1, 151-168.

[28] Jones, N. 1973. Slamming Damage. Journal of Ship Research, 17, 2, 80-86.

[29] Bereznitski, A. 2001. Slamming: the role of hydroelasticity. International Shipbuilding Progress, 48, 4, 333-351.

[30] Stenius, I. 2006. Explicit fe-modelling of fluid–structure interaction in hull-water impacts. International Shipbuilding Progress, 53, 2, 103-121.

[31] Stenius, I., Rosén, A., Kuttenkeuler, J. 2007. Explicit fe-modelling of hydroelasticity in panel-water impacts. International Shipbuilding Progress, 54, 2-3, 111-127.

[32] Panciroli, R., Porfiri, M. 2013. Evaluation of the pressure field on a rigid body entering a quiescent fluid through particle image velocimetry. Experiments in Fluids, 54, 1630. https://doi.org/10.1007/s00348-013-1630-3.

[33] Shams, AM., Jalalisendi, Porfiri, M. 2015. Experiments on the water entry of asymmetric wedges using particle image velocimetry. Physics of Fluids, 27, 027103. https://doi.org/10.1063/1.4907745.

[34] Panciroli, R. 2012. Hydroelastic Impacts of Deformable Wedges. PhD Thesis of University of Bologna.

[35] Metschkow, B. 2006. Sandwich panels in shipbuilding. Polish Maritime Research, 13(S1), 5-8.

[36] Kujala P., Klanac A. 2005. Steel sandwich panels in marine applications. Brodogradnja/ Shipbuilding: Theory and Practice of Naval Architecture, Marine Engineering and Ocean Engineering, 56, 4, 305-314.

[37] Kozak, J. 2009 Selected problems on application of steel sandwich panels to marine structures. Polish Maritime Research, 16, 4, 9-15. https://doi.org/10.2478/v10012-008-0050-4.

[38] Deshpande, VS., McShane, GJ., Fleck, NA. 2007. The underwater blast resistance of metallic sandwich beams with prismatic lattice cores. Journal of Applied Mechanics, 74, 2, 352-364.
https://doi.org/10.1115/ 1.2198549.

[39] Cheng YS., Zhou TY., Wang H., *et al*. 2017. Numerical investigation on the dynamic response of foam-filled corrugated core sandwich panels subjected to air blast loading. Journal of Sandwich Structures and Materials, 21, 3, 838-864. https://doi.org/ 10.1177/1099636217700350.

[40] Zhang, P., Cheng, YS., Liu, J., *et al*. 2015. Experimental and numerical investigations on laser-welded corrugated-core sandwich panels subjected to air blast loading. Marine Structures, 40, 225-246.
https://doi.org/10.1016/j.marstruc.2014.11.007.

[41] Zhang, P., Cheng, Y.S., Liu, J., *et al*., 2015. Dynamic response of metallic trapezoidal corrugated-core sandwich panels subjected to air blast loading-An experimental study. Materials and Design, 65, 221-230. https://doi.org/10.1016/j.matdes.2014.08.071.

[42] Wang, H., Cheng, YS., Liu, J., *et al*. 2016. The fluid-Solid interaction dynamics between underwater explosion bubble and corrugated sandwich plate. Shock and Vibration, Article ID 6057437, 1-21.
http://dx.doi.org/10.1155/2016/6057437.

[43] Wang, H., Zhao, F., Cheng, YS., *et al*. 2012. Dynamic response analysis of light weight pyramidal sandwich plates subjected to water impact. Polish Maritime Research, 19, 4, 31-43.
https://doi.org/10.2478/v10012-012-0038-y.

[44] Wang, H., Cheng, YS., Liu, J. 2013. 3D Dynamic hydroelasticity analysis of light weight pyramidal sandwich plates with imperfection subjected to water impact. Proceedings of 4th International Conference on Mechanical and Aerospace Engineering, Moscow, Russia, 266-272. https://doi.org/10.4028/www.scientific.net/AMM.390.266.

[45] Wallach, JC., Gibson, LJ. 2001. Mechanical behaviour of a three-dimensional truss material. International Journal of Solids and Structures, 38, 40-41, 7181–7196. https://doi.org/10.1016/S0020-7683(00)00400-5.

[46] Bolotin. BB. 1960. Calculation of strength. 1960, 6(6), Mashgiz. (Болотин ВВ. Расчёт на прочность, вьі (6), Машгиз, 1960). (In Russian).

[47] Institute of Mechanics, Chinese Academy of Sciences. 1977. Bending, Vibration and Stability of Sandwich Plates and Shells. Beijing, Science Press. (In Chinese).

[48] Korobkin, AA., Pukhnachov, VV. 1985. Initial asymptotic in contact hydrodynamics problem. Proceedings of 4th International Conference on Numerical Ship Hydrodynamics, Washington D.C., USA, 138-151.

[49] Korobkin, AA., Pukhnachov, VV. 1988. Initial stage of water impact. Annual Review of Fluid Mechanics, 20, 159-185. https://doi.org/10.1146/annurev.fl.20.010188.001111.

[50] Campana, EF., Carcaterra, A., Ciappi, E., *et al*. 2000. Parametric analysis of slamming forces compressible and incompressible Phases. Journal of Ship & Ocean Technology, 4, 1, 21-27.

Submitted: 24.10.2017.
Accepted: 21.03.2019.

Corresponding author, Hao Wang, wanghao818489@163.com
China Institute of Marine Technology & Economy, Peking 100081,PR China
Cheng Yuan-Sheng, *School of Naval Architecture and Ocean Engineering, Huazhong University of Science and Technology, Wuhan 430074, PR China*
Pei Da-Ming, *China Institute of Marine Technology & Economy, Peking 100081, PR China*
Hao Wei-Wei, *China Institute of Marine Technology & Economy, Peking 100081, PR China*
Gan Lin, *Wuhan Secondary Ship Design & Research Institute, Wuhan 430074, PR China*